Atmospheric and Oceanic Science Letters 18 (2025) 100672

Contents lists available at ScienceDirect

Atmospheric and Oceanic Science Letters

journal homepage: http://www.keaipublishing.com/en/journals/atmospheric-and-oceanic-science-letters/

The extreme windstorm of April 2025 in northern and central-eastern China: Historical ranking and synoptic origins

Shenming Fu[a,b,*], Tingting Huang[b], Bo Wang[c], Xiao Li[d], Nan Zhang[e], Zhongcan Chen[f], Jingxue Wang[f], You Dong[g], Jianhua Sun[b]

[a] *National Key Laboratory of Earth System Numerical Modeling and Application, Institute of Atmospheric Physics, Chinese Academy of Sciences, Beijing, China*
[b] *Laboratory of Cloud–Precipitation Physics and Severe Storms, Institute of Atmospheric Physics, Chinese Academy of Sciences, Beijing, China*
[c] *State Key Laboratory of Renewable Energy Grid-Integration, China Electric Power Research Institute, Beijing, China*
[d] *School of Civil Engineering, Chongqing University, Chongqing, China*
[e] *Hebei Meteorological Bureau, Shijiazhuang, China*
[f] *School of Soil and Water Conservation, Beijing Forestry University, Beijing, China*
[g] *Department of Civil and Environmental Engineering, The Hong Kong Polytechnic University, Hong Kong, China*

ARTICLE INFO

Keywords:
Strong wind
Cold vortex
Cyclone
Mesoscale vortex
Kinetic energy

关键词:
大风
冷涡
气旋
中尺度涡旋
动能收支

ABSTRACT

In mid-April 2025, northern and central-eastern China experienced a catastrophic compound disaster marked by Beaufort 8 or greater wind gusts affecting ~3.5×10^6 km^2, exposing ~610 million residents to extreme conditions, with Typhoon-equivalent Beaufort 12 gusts battering Beijing's Yanshan Mountains and Beaufort 14–15 winds devastating Inner Mongolia. This unprecedented event surpassed historical extremes at 64 weather stations, impacting 996 monitoring sites with winds exceeding the 99th percentile, including 478 stations recording historic top-three maxima. Concurrently, sandstorms engulfed ~4.3×10^6 km^2, reaching 18°N, while Hulunbuir faced a 1.5-m snowpack—a 30-year April record. Cascading infrastructure failures resulted in 1884 uprooted trees, approximately ¥16.6 million in urban damages (in Beijing), and the collapse of utility-scale photovoltaic systems across northern China and the Huang-Huai region, exacerbating the multi-faceted crisis. A brief analysis indicates the event was primarily driven by a vertically coupled cyclone system featuring a cold vortex at the middle and upper troposphere dynamically aligned with a lower-level cyclone/mesoscale vortex. The intense, deeply coupled cyclone system sustained the wind intensification primarily through its enhanced pressure gradient force and subsidence-induced downward transport of kinetic energy (KE) behind the cyclone's core. Clarifying the controlling synoptic-scale weather systems and dominant physical mechanisms governing such extreme wind generation is critical for refining predictive models of these high-impact events while advancing the understanding of dynamic interactions within extreme wind regimes.

摘要
2025年4月中旬, 中国北部和中东部地区遭遇由8级以上阵风引发的复合型灾害, 影响范围约3.5×10^6平方公里, 波及约6.1亿人口. 北京燕山山脉出现12级 (台风级) 阵风, 内蒙古局部地区风力达14–15级. 此次事件在64个气象站突破历史极值, 996个监测站点风速超过第99百分位 (478个站点创观测史前三极值) . 伴随沙尘暴影响范围达4.3×10^6平方公里, 南扩至18°N; 呼伦贝尔出现1.5米积雪, 为30年来4月最深纪录. 灾害导致1884株树木倒伏, 北京城市设施损失约1660万元, 并造成华北, 黄淮地区光伏系统大面积损毁. 研究表明, 该事件由垂直耦合气旋系统驱动, 中高层冷涡与低层气旋/中尺度涡旋动力耦合, 通过增强气压梯度及下沉动能传输维持强风. 阐明此类极端风的天气系统及物理机制, 对改进预测模型及深化风场动力学认知具有重要意义.

1. Introduction

From 11 to 14 April 2025, an exceptionally rare and prolonged extreme windstorm event impacted northern and central-eastern China. The event was characterized by an unprecedented spatial extent, duration, and wind intensity (Committee of Wind Disaster Mitigation and Energy Utilization, 2025). The storm affected an area exceeding 3.5 million square kilometers, directly impacting more than 610 million people. Major regions, including Beijing, Hebei, and Inner Mongolia, endured hurricane-force gusts exceeding Beaufort 8 scale for over 15 consecu-

---

[*] Corresponding author.
E-mail address: fusm@mail.iap.ac.cn (S. Fu).

https://doi.org/10.1016/j.aosl.2025.100672
Received 13 May 2025; Revised 21 May 2025; Accepted 26 June 2025

tive hours. Notably, 64 national-level meteorological stations recorded historically unprecedented wind speeds. In mountainous areas, winds reached typhoon-equivalent intensities (Beaufort 12), while parts of Inner Mongolia experienced extreme gusts of Beaufort 14–15. The extreme wind event was compounded by concomitant meteorological hazards including precipitous temperature declines, intense snowfall, and extensive sandstorm activity, with these multi-hazard interactions significantly amplifying disaster impacts through synergistic effects.

During the event, concurrent sandstorms, triggered by the gales, spread as far as northern Hainan Island (https://baike.baidu.com/item/2025%E5%B9%B44%E6%9C%88%E5%8D%8E%E5%8C%97%E5%BC%BA%E9%A3%8E/65576125), affecting over ~4.3 million square kilometers. Severe sandstorms struck western Inner Mongolia and central Gansu, and marked the most significant sandstorm impact on Guangdong in 15 years. Inner Mongolia's Hulunbuir border region faced its most intense April snowstorm in a decade, with 1.5-m snow accumulations causing highway blockages (https://www.news.cn/fortune/20250415/83e7932406ae4611853fb20713e8f91e/c.html). Local authorities activated an extreme cold weather emergency rescue plan, relocating ~1000 stranded residents and sheltering over 4000 livestock.

Beijing emerged as one of the most severely impacted regions during this extreme wind event (Fig. 1(a–f)), with municipal authorities documenting ~1884 instances of complete tree uprooting and ~5065 cases of branch fracture (Committee of Wind Disaster Mitigation and Energy Utilization, 2025), resulting in cascading effects that included vehicular crushing incidents, power line disruptions, and structural impairments to residential buildings. The socioeconomic consequences proved significant, as evidenced by insurance claims for property damage in the capital reaching ~16.6 million yuan.

The extreme wind event also exerted substantial impacts on photovoltaic systems across northern and central-eastern China and the Huang-Huai region (https://www.sohu.com/a/883643475_121956424). Widespread structural failures occurred, including dislodged solar panels, deformed rooftop mounts, and compromised structural supports. State Grid implemented comprehensive emergency measures (http://www.sgcc.com.cn/html/sgcc_main/gb/xwzx/yw/20250412/8048622025041216160000001.shtml), with State Grid's Eastern Inner Mongolia branch intensifying ultra-high-voltage line inspections and anti-icing protocols, while Gansu reinforced transmission corridors against sandstorms.

In summary, this unprecedented windstorm event of 11–14 April 2025 has attracted significant multidisciplinary attention due to its widespread societal consequences. It has prompted critical examination by policymakers, affected communities, and researchers. Two fundamental scientific questions have emerged from this discourse: (i) How extreme was this windstorm event? (ii) What are the underlying mechanisms responsible for the formation of such extreme winds? After describing the data and methods used in the study in Section 2, these questions are discussed in Sections 3 and 4, respectively.

2. Data and methods used in the study

This study employed three distinct datasets: (i) The 0.25° × 0.25° hourly ERA5 reanalysis (Hersbach et al., 2020), which served as the primary data source for synoptic-scale diagnostic analysis and KE budget calculations. (ii) Surface wind observations from the China Meteorological Administration's station network, with varying station densities over the 75-year spring period (1951–2025), which enabled temporal characterization of windstorm evolution and assessment of the historical extremeness through percentile ranking analysis. (iii) High-resolution (15 arc-second) global topographic data from the General Bathymetric Chart of the Oceans (https://www.gebco.net/data_and_products/gridded_bathymetry_data), which facilitated terrain feature characterization, particularly for regions with lower altitudes.

The KE budget diagnostics, an established methodological framework for elucidating the fundamental dynamics of wind variability (Fu et al., 2020; Ma et al., 2022), are mathematically formulated in the isobaric coordinate system as follows:

$$\frac{\partial k_{\mathrm{h}}}{\partial t} = \underbrace{u\frac{k_{\mathrm{h}}}{\partial x} - v\frac{k_{\mathrm{h}}}{\partial y}}_{\mathrm{HAV}} \underbrace{-\omega\frac{k_{\mathrm{h}}}{\partial p}}_{\mathrm{VAV}} \underbrace{-u\frac{\partial \boldsymbol{\Phi}}{\partial x} - v\frac{\partial \boldsymbol{\Phi}}{\partial y}}_{\mathrm{WPG}} + \mathrm{RES}\#, \tag{1}$$

where $k_{\mathrm{h}} = \frac{1}{2}(u^2 + v^2)$ represents the horizontal KE, ω denotes the vertical velocity in pressure coordinates, and $\boldsymbol{\Phi}$ is geopotential. The local temporal KE tendency $\frac{\partial k_{\mathrm{h}}}{\partial t}$ is governed by three principal dynamic processes: horizontal KE advection (HAV), characterizing wind-driven lateral transport; vertical KE advection (VAV), representing energy transfer through vertical motion; and work performed by the pressure gradient force on horizontal winds (WPG). The residual term (RES) in Eq. (1) incorporates contributions from numerical discretization errors, subgrid-scale processes, and frictional dissipation. For diagnostic purposes, we define the composite term TOT as the summation of HAV, VAV, and WPG, which collectively represents the aggregate dynamic forcing on KE budgets, excluding the residual effects.

3. Historical ranking

In this study, the number of stations available for analysis varies across different years, ranging from a minimum of 140 (1951–1952) to a maximum of 2598 (2018–2025). Statistical analysis shows that on 11–13 April 2025, the number of stations recording daily maximum wind speeds above the 99th percentile reached 251, 996, and 309, respectively (Fig. 1(g–i)). Furthermore, the counts of stations achieving historically top-3 maximum wind speeds for these dates were 88, 478, and 104. In contrast, significantly weaker wind speeds were recorded on 10 and 14 April 2025 (not shown), corresponding to the incipient and dissipating phases of the event, respectively.

For the five stations exhibiting the most extreme wind speeds nationwide during each day of the event (Table 1), on 11 April 2025, three stations (53601, 57635, 58529) recorded their highest spring wind speeds in the 75-year observational record (1951–2025). This was followed by three additional stations (54287, 54308, 54630) achieving similar record-breaking intensities on 12 April 2025, while only one station (53690) reached its historical spring maximum on 13 April 2025. All these demonstrate the extraordinary intensity of this extreme wind event.

4. Synoptic origins

4.1. Synoptic analysis

The upper-tropospheric evolution of the event featured a rapidly intensifying shortwave trough propagating eastward (Fig. 2(a, b)), with development mainly occurring from 0800 Beijing Time (BJT) 11 April to 0800 BJT 14 April 2025, as evidenced by sustained geopotential height falls (not shown). Then, after 0800 BJT 14 April, the trough was mainly located over the sea and began to weaken. The trough developed a closed circulation center at approximately 0800 BJT 13 April 2025 (Fig. 2(b)), maintaining this configuration for ~24 h, indicative of the cold vortex's intensification. Behind the trough axis, robust northerly winds facilitated the southward advection of cooler air masses (Fig. 2(a and b)), while ahead of the trough, pronounced upper-level divergence prevailed, providing sustained support for ascending motion.

In the middle troposphere, a distinct shortwave trough was observed at the 500 hPa level (Fig. 2(c, d)), exhibiting spatial correspondence with the upper-tropospheric trough. This 500 hPa trough demonstrated consistent eastward movement and gradual intensification, mirroring the evolutionary characteristics of the 200 hPa trough. At around 0800 BJT 12 April, the system developed into a well-defined closed geopotential

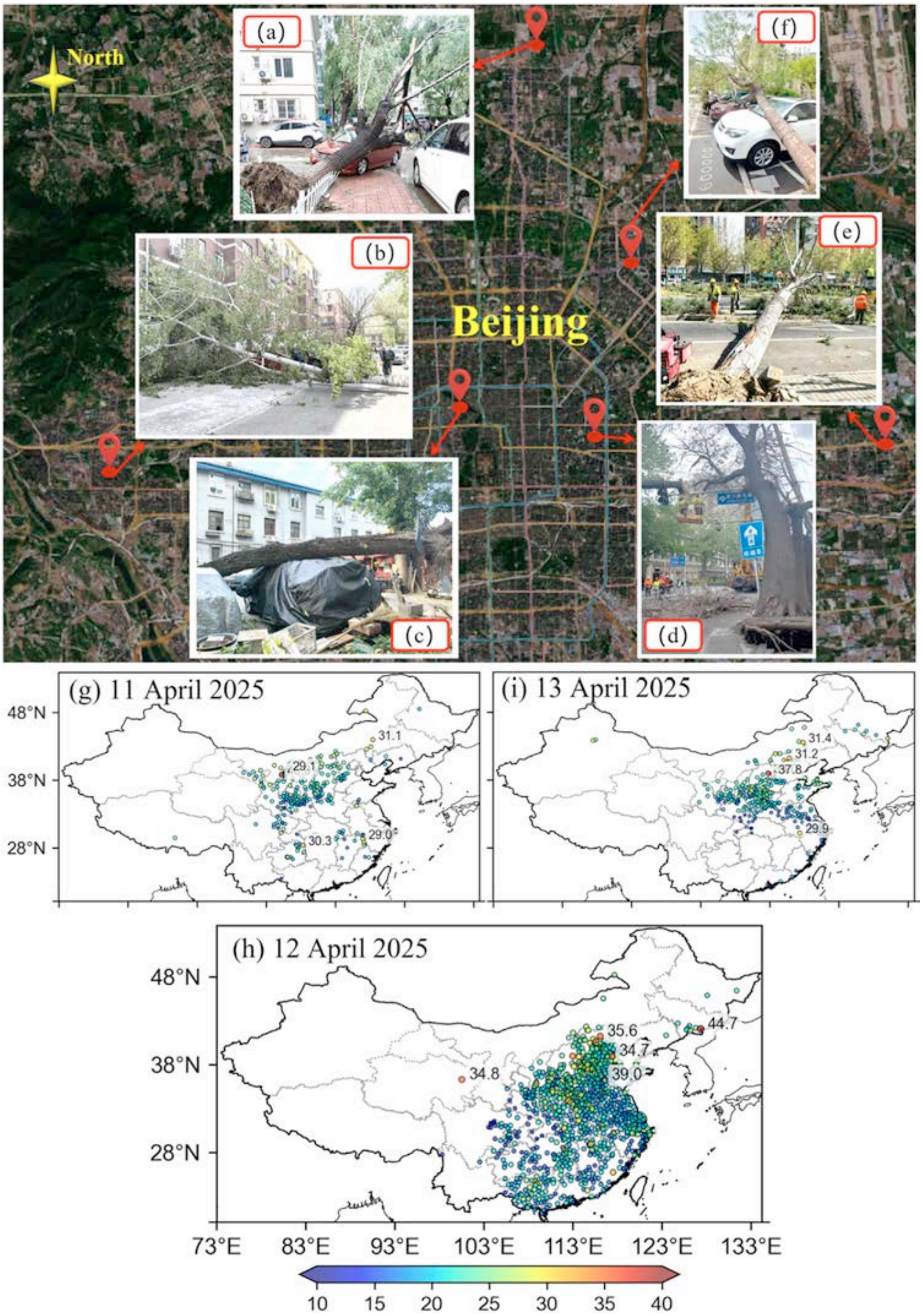

Fig. 1. (a–f) Disaster scenarios in different locations of Beijing (12 April 2025). (g) Daily maximum wind speeds (shaded dots; units: m s^{-1}) recorded during the event, which ranked in the top 1 % of historical observations at the stations (spring, 1951–2024). The numbers highlight the top five stations with the highest recorded wind speeds across China on 11 April 2025. (h, i) As in (g) but for 12 and 13 April 2025, respectively.

height center (Fig. 2(c)), marking the formation of the cold vortex. Notably, a pronounced cold core (−35 °C) became established near the vortex center ~24 h prior to its manifestation at 200 hPa (not shown). During the period from 0800 BJT 12 to 2000 BJT 13 April 2025, the cold vortex exhibited eastward movement with concurrent intensification. Subsequently, commencing at 0800 BJT 14 April, the vortex initiated a weakening phase, ultimately dissipating at approximately 1600 BJT 15 April (not shown). The emergence of a closed geopotential height center at 200 hPa, observed between 0800 BJT 13 April and 0800 BJT 14 April 2025 (Fig. 2(b)), can be attributed to the vertical extension of the 500 hPa cold vortex.

In the lower troposphere, a cyclone/mesoscale-vortex (Fu et al., 2020) developed at around 0500 BJT 11 April 2025 (not shown), forming ahead of the shortwave trough in the middle and upper troposphere. The cyclone moved eastward while gradually intensifying and extending vertically (Fig. 2(e–m)). By 0800 BJT 12 April 2025, the cyclone had established full vertical coupling with the mid- to upper-tropospheric cold vortex (Fig. 2(c, f)). Subsequently, the coupled cyclone system migrated eastward while continuing to develop, before ultimately dissipating at around 1600 BJT 15 April 2025 (not shown). The system attained its maximum vertical extent, spanning the entire troposphere, between 0800 BJT 13 April and 0800 BJT 14 April 2025 (Fig. 2(b, d, and j)).

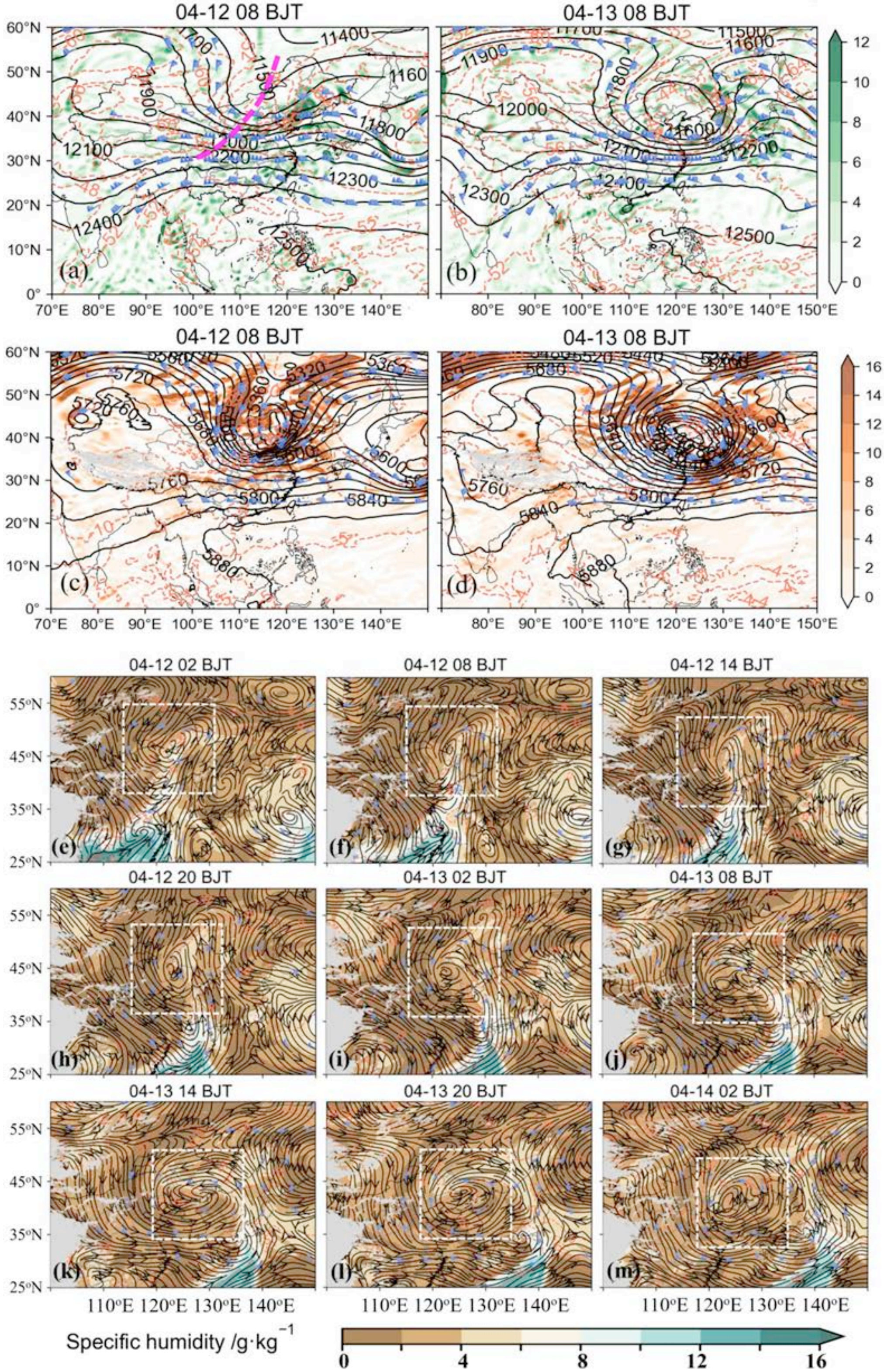

Fig. 2. (a, b) The divergence (shading; units: 10^{-5} s^{-1}), wind (above 25 m s^{-1}; a full barb is 10 m s^{-1}), geopotential height (black contours; units: gpm), and temperature (red contours; units: K) at 200 hPa at 0800 BJT 12 April and 0800 BJT 13 April 2025, respectively, where the thick dashed purple line represents the trough line. (c, d) The temperature advection (shading; units: 10^{-5} K s^{-1}), wind (above 15 m s^{-1}; a full barb is 10 m s^{-1}), geopotential height (black contours; units: gpm), and temperature (red contours; units: K) at 500 hPa at 0800 BJT 12 April and 0800 BJT 13 April 2025, respectively, where the gray shading highlights the regions above 5000 m. (e) The specific humidity (shading; units: g kg^{-1}), temperature (red contours; units: K), wind (above 12 m s^{-1}; a full barb is 4 m s^{-1}), and stream field at 850 hPa at 0200 BJT 12 April 2025, where the gray shading highlights the regions above 1500 m, and the white dashed box outlines the main body of the cyclone/mesoscale-vortex (determined by the temporal mean size of the cyclone throughout its complete lifecycle). (f–m) As in (e) but for the following moments (at 6-h intervals).

Table 1 Maximum wind speed characteristics at China's five most extreme wind-affected stations during the 11–13 April 2025 event (Fig. 2), with bold typeface highlighting the maximum historical wind speed. The threshold is defined as the 99th percentile value in the statistical distribution of daily maximum wind speeds.

Date	Station ID	Longitude (°E)	Latitude (°N)	Altitude (m)	Direction (°)	Speed (m s^{-1})	Threshold	Max wind speed (m s^{-1})
11 April 2025	53601	105.90	38.77	2908.00	315	**46.00**	37.74	**46.00**
	54027	119.32	43.96	587.80	239	31.10	30.44	44.60
	57635	109.02	28.37	548.70	290	**30.30**	15.90	**30.30**
	52607	106.66	39.43	1252.80	329	29.10	23.64	34.70
	58529	117.86	29.28	166.90	252	**29.00**	17.44	**29.00**
12 April 2025	54287	128.07	42.03	2620.00	76	**44.70**	41.10	**44.70**
	54826	117.11	36.26	1521.20	332	39.00	34.35	40.40
	54308	116.63	41.20	734.80	317	**35.60**	26.30	**35.60**
	52859	100.90	36.29	3816.00	5	34.80	29.16	36.70
	54630	117.98	38.94	38.30	12	**34.70**	31.97	**34.70**
13 April 2025	53588	113.51	38.94	2208.30	270	39.00	33.84	43.40
	53690	114.21	38.87	328.50	296	**37.80**	24.50	**37.80**
	54113	118.63	43.53	688.80	340	31.40	30.87	38.20
	54308	116.63	41.20	734.80	318	31.20	26.30	35.60
	58437	118.16	30.13	1839.70	326	29.90	28.34	34.70

Both the lower-tropospheric cyclone/mesoscale-vortex (which mainly affected 11 April 2025) and the coupled cyclone system (which mainly affected 12–14 April 2025) served as the principal synoptic-scale drivers of the extreme wind event.

4.2. KE budget

To investigate the formation mechanisms of the extreme winds, we conducted a KE budget analysis, as KE serves as a direct indicator of wind intensity. The KE budget was calculated using 0.25° × 0.25° ERA5 data, then averaged within 0.5° × 0.5° grid boxes centered on selected meteorological stations to represent both the stations and their immediate surrounding areas. The station selection criterion was based on maximum recorded wind speeds in northern and central-eastern China during the study period: station 53601 (11 April 2025), station 54308 (12 April 2025), and station 53588 (13 April 2025). These stations exhibited the peak wind speed measurements for their respective days in the northern and central-eastern China region (Fig. 3). An evaluation of the KE budget terms reveals that the ratios of the local temporal KE tendency to term TOT average approximately 0.71 (not shown). This suggests that the balance in Eq. (1) is acceptable for further analysis (Fu et al., 2019, 2022).

For Station 53601 on 11 April 2025, the maximum observed wind speed reached approximately 46.0 m s^{-1} (Fig. 3(a)), which is the strongest of China in the day. Analysis of the KE budget reveals that term TOT exhibited pronounced positive values extending from the surface to 200 hPa prior to the wind speed maximum (Fig. 4(d)). This enhancement can be primarily attributed to the combined effects of the lower-tropospheric cyclone/mesoscale-vortex, which generated reduced surface pressure, and a mid- to upper-tropospheric shortwave trough. Terms WPG and VAV constituted the first and second most significant positive contributions, respectively, while HAV generally exhibited an opposing effect, as it caused a net-export transport of KE. This finding indicates that the pressure gradient force associated with the lower-tropospheric cyclone served as the dominant mechanism in generating the extreme wind event. Additionally, downward KE transport played a substantial role, with its origin traceable to the mid- and upper troposphere (Fig. 4(b, f)), where WPG also exerted dominant influence.

For Station 54308 on 12 April 2025, the maximum observed wind speed reached approximately 35.6 m s^{-1} (Fig. 3(b)), representing the most intense wind event recorded in northern China that day. As Fig. 4(j) shows, a pronounced positive TOT was predominantly observed below 500 hPa prior to the development of the extreme wind event. Terms VAV and WPG were the primary and secondary contributors, respectively (Fig. 4(h, i)), whereas the HAV term primarily acted to attenuate the strong winds (Fig. 4(g)). The dominant mechanism was identified as the downward KE transport from the mid-troposphere (Fig. 4(h, l)), where KE intensification was primarily driven by horizontal KE transport (Fig. 4(g)). Secondary contributions arose from the work performed by the pressure gradient force associated with the coupled cyclone.

For Station 53588 on 13 April 2025, the maximum observed wind speed reached approximately 39.0 m s^{-1} (Fig. 3(c)), representing the most intense wind event recorded in China that day. Comparative analysis of the budget terms reveals that terms VAV and WPG contributed nearly equally to wind enhancement (Table 2), whereas HAV predominantly decelerated the strong winds. The downward KE transport originated from the middle and upper troposphere (not shown), where KE amplification was mainly driven by horizontal KE transport.

As Table 2 shows, during the extreme wind event of 11–13 April 2025, the primary common features involve consistent contributions from both WPG and VAV to wind intensification, while HAV predominantly acted to decelerate wind acceleration. The positive WPG component was fundamentally driven by the pressure gradient force associated with the cyclone/vortex. The downward KE transport, manifested as positive VAV, principally occurred due to the prevalence of descending motions in the region behind the mid-tropospheric shortwave trough where the maximum winds were observed. These descending motions, extending to near-surface levels, generated divergent flow patterns that facilitated net KE export, corresponding to negative HAV values. Key distinctions emerge in the relative contributions of WPG and VAV, which exhibit significant variation depending on the spatial positioning and temporal evolution of the cyclone/vortex. Additionally, the vertical extent of layers exhibiting substantial downward KE transport demonstrates marked differences in their respective thicknesses.

5. Discussion and summary

Climatological analyses reveal a distinct spatial predominance of high wind events across northern and central-eastern China, with peak occurrence frequencies during winter and spring seasons (Ding et al., 2019; Li et al., 2022). However, observational records demonstrate a significant decelerating trend in surface wind speeds throughout these regions in recent decades (Nan et al., 2024), where daily peak wind velocities demonstrate disproportionately stronger diminishing trends (Nan et al., 2024). However, this observed wind speed attenuation does not necessarily translate to reduced intensity of extreme wind events in northern and central-eastern China, as evidenced by the extreme wind event of mid-April 2025 discussed in this article.

In contrast to warm-season strong winds predominantly attributed to severe convective processes (Qin et al., 2006; Markowski and Richardson, 2010; Fu et al., 2019; Wagner et al., 2025) and tropical cyclone activity (Guo and Tan, 2017; Walsh et al., 2020; Tsukada and Horinouchi, 2023), cold-season wind extremes exhibit distinct dynamic origins, primarily associated with extratropical cyclones, cold

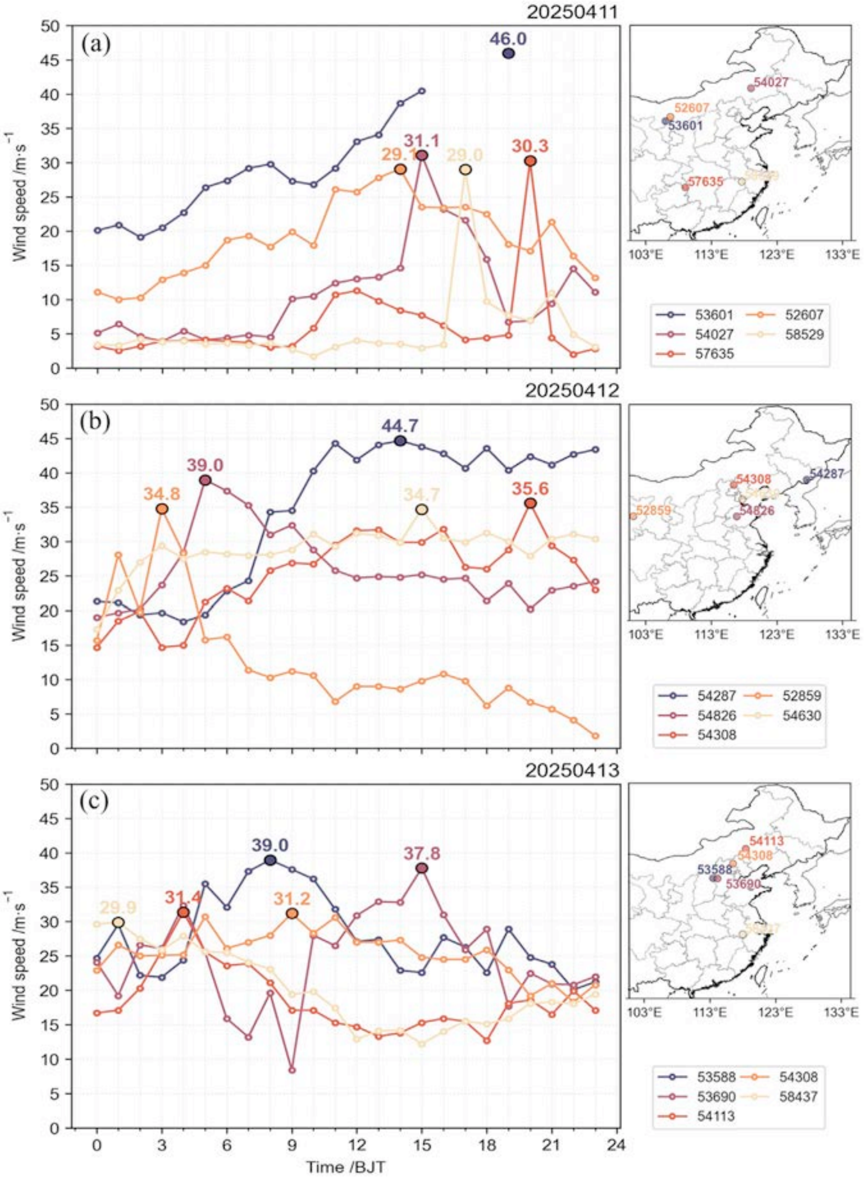

Fig. 3. (a) The 24-h variation in wind speed at the stations recording the top five highest wind speeds across China on 11 April 2025. The numbers on the left indicate the maximum wind speeds, while those on the right correspond to the station IDs. (b, c) As in (a) but for 12 and 13 April 2025, respectively.

Table 2 Dominant, secondary, and detrimental factors of the extreme winds: station 53601 (11 April 2025), station 54308 (12 April 2025), and station 53588 (13 April 2025). The locations of the maximum wind relative to the vortex/cyclone are also shown. Quadrants are defined as the four congruent sub-rectangles formed by two orthogonal bisectors intersecting at the geometric center of the blue dashed box (Fig. 4).

	11 April 2025	12 April 2025	13 April 2025
Dominant factors	WPG	VAV	VAV and WPG
Secondary factors	VAV	WPG	/
Detrimental factors	HAV	HAV	HAV
Locations relative to vortex/cyclone	Southwest of the mesoscale vortex	Southwestern quadrant	West of the coupled cyclone

vortices, lower-pressure troughs, and surface high-pressure systems (Fu et al., 2012, 2024; Yamada and Hirasawa, 2018; Brâncus et al., 2019; McClung and Mass, 2020; Tsai et al., 2022). Under a warming climate, as colder air masses are advected equatorward by extratropical cyclones, they encounter significantly warmer air in lower latitudes, thereby amplifying the meridional temperature gradient. This strengthened thermal contrast directly intensifies the baroclinic zone, which serves as the fundamental energy source for the rapid development of cyclones (Jiang et al., 2021; Hirata et al., 2021). Consequently, the enhanced baroclinicity generates more vigorous extratropical cyclones characterized by steeper pressure gradients, which produce stronger winds. This dynamic mechanism provides the synoptic-scale explanation for the extreme wind event of mid-April 2025.

In addition to synoptic-scale dynamic forcing, orographic effects contribute substantially to high wind generation, especially in topographically complex regions. For instance, Ding et al. (2019) and Xi et al. (2022) found the topography of the Tianshan Grand Canyon channels and accelerates northwesterly/westerly winds through orographic forcing, with downslope windstorms arising from nonlinear high-drag regimes and hydraulic jump-like dynamics as flow transitions

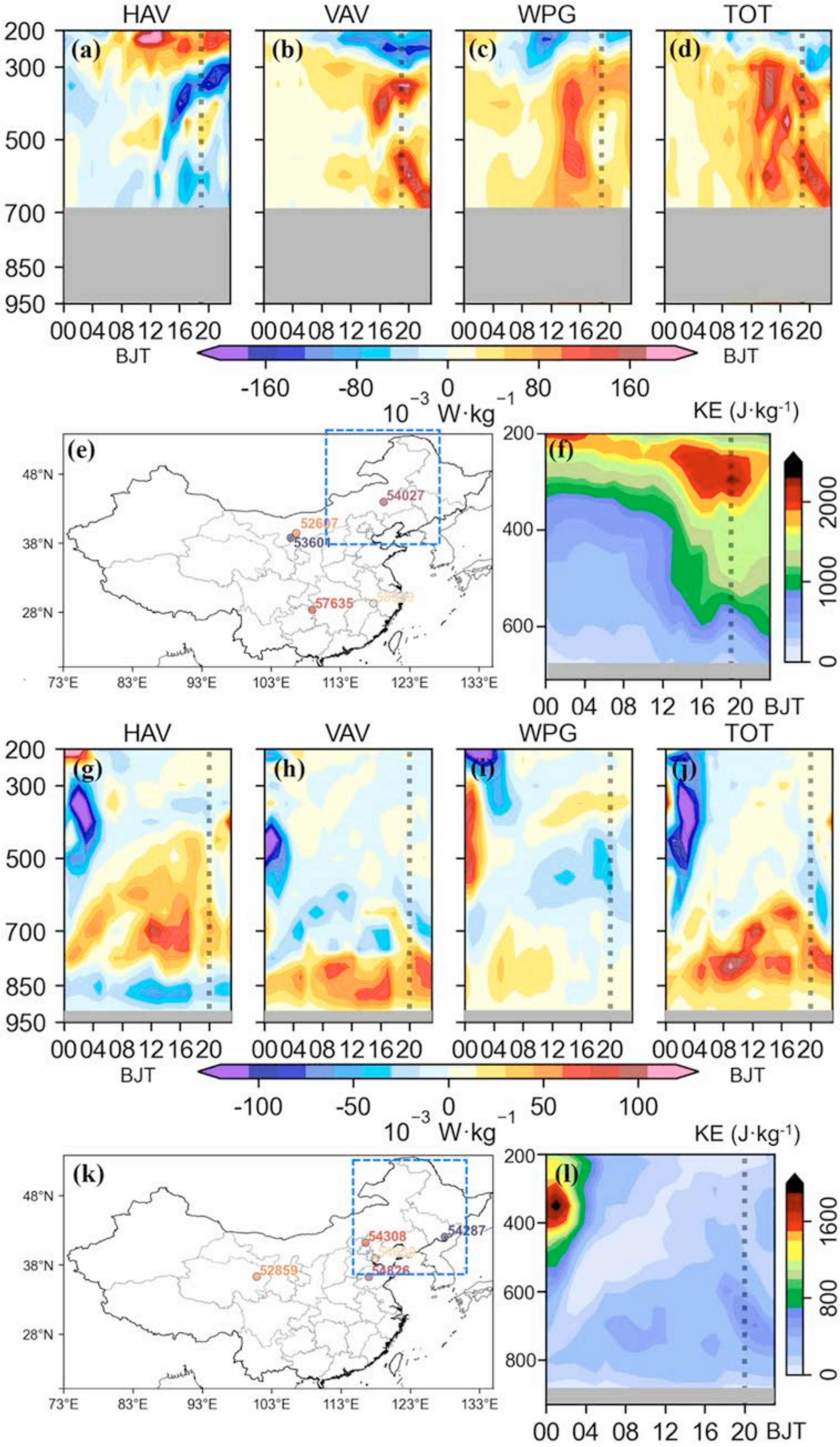

Fig. 4. (a–d) The 24-h variation in KE budget terms (shading; units: 10^{-3} W kg^{-1}) averaged over a 0.5° × 0.5° box centered at station 53601 on 11 April 2025. Gray shading indicates the station altitude, and gray dashed lines mark the time of maximum wind speed. (e) The top five stations with the highest recorded wind speeds across China on 11 April 2025, with the blue dashed box highlighting the main body of the mesoscale vortex at peak wind conditions. (f) The mean KE (shading; units: J kg^{-1}) within the same 0.5° × 0.5° box around station 53601, with gray shading again denoting altitude and dashed lines indicating the time of maximum wind. (g–l) As in (a–f) but for the coupled cyclone (blue dashed box) on 12 April 2025.

from subcritical to supercritical over the lee slope. The canyon's terrain enhances pressure gradients and generates critical layers, triggering unstable stratification and sinking motions that intensify southeasterly gales near its northwest opening, as observed in the 2013 Urumchi event.

To address the escalating challenges posed by cold-season wind extremes in northern and central-eastern China under a warming climate, a three-part strategy is proposed: (i) Develop advanced multiscale prediction systems combining high-resolution terrain modeling, boundary layer physics, and machine learning–enhanced ensemble forecasting for precise risk assessment. (ii) Investigate climate-wind linkages via multidisciplinary research integrating mesoscale modeling, urban-terrain coupling experiments, and satellite evaluation of ecological interventions, focusing on anthropogenic influences on pressure systems. (iii) Implement risk communication frameworks using VR hazard visualization, community capacity building, and citizen science sensor networks for localized early warnings.

Funding

This research was supported by the National Natural Science Foundation of China [grant number 42475008] and the Strategy Priority Research Program of the Chinese Academy of Sciences [grant number XDB0760400].

Acknowledgments

The authors thank the ECMWF and China Meteorological Administration for providing the data.

References

Brâncuş, M., Schultz, D.M., Antonescu, B., Dearden, C., Ştefan, S., 2019. Origin of strong winds in an explosive Mediterranean extratropical cyclone. Mon. Wea. Rev. 147, 3649–3671. doi:10.1175/MWR-D-19-0009.1.

Committee of Wind Disaster Mitigation and Energy Utilization, 2025. Damage survey report of extreme wind event in Beijing on 11 April 2025 [Available online at. https://mp.weixin.qq.com/s/ECXL_dz0rNn_EwUKhr8Wbg (in Chinese).

Ding, J., Chen, Y., Wang, Y., Xu, X., 2019. The southeasterly gale in Tianshan grand canyon in Xinjiang, China: A case study. J. Meteorol. Soc. Jpn. 97, 55–67. doi:10.2151/jmsj.2019-002.

Fu, S.-M., Mai, Z., Sun, J.-H., Li, W.-L., Ding, Y., Wang, Y.-Q., 2019. Impacts of convective activity over the Tibetan Plateau on plateau vortex, southwest vortex, and downstream precipitation. J. Atmos. Sci. 76, 3803–3830. doi:10.1175/JAS-D-18-0331.1.

Fu, S.-M., Zhao, S.-X., Sun, J.-H., Qi, L.-L., 2012. Energy budget of a cold surge process during the winter monsoon period of 2004. Clim. Environ. Res. 17, 549–562. doi:10.3878/j.issn.1006-9585.2011.10114, (in Chinese).

Fu, S.-M., Zhang, J.-P., Tang, H., Jiang, L.-Z., Sun, J.-H., 2020. A new mesoscale-vortex identification metric: restricted vorticity and its application. Environ. Res. Lett. 15, 124053. doi:10.1088/1748-9326/abcac6.

Fu, S.-M., Zhang, Y.-C., Wang, H.-J., Tang, H., Li, W.-L., Sun, J.-H., 2022. On the evolution of a long-lived mesoscale convective vortex that acted as a crucial condition for the extremely strong hourly precipitation in Zhengzhou. J. Geophys. Res.: Atmos. 127, e2021JD036233. doi:10.1029/2021JD036233.

Fu, S.-M., Ma, H., Jiang, L.-Z., 2024. Increasing risks of the explosive extratropical cyclones over the North Atlantic storm track: A perspective from their surface wind maxima. Environ. Res. Lett. 19, 054009. doi:10.1088/1748-9326/ad3b24.

Guo, X., Tan, Z.-M., 2017. Tropical cyclone fullness: A new concept for interpreting storm intensity. Geophys. Res. Lett. 44, 4324–4331. doi:10.1002/2017GL073680.

Hersbach, H., Bell, B., Berrisford, P., Hirahara, S., Horanyi, A., Munoz-Sabater, J., Nicolas, J., et al., 2020. The ERA5 global reanalysis. Q. J. R. Meteorol. Soc. 146 (730), 1999–2049. doi:10.1002/qj.3803.

Hirata, H., 2021. Climatological features of strong winds caused by extratropical cyclones around Japan. J. Clim. 34, 4481–4494. doi:10.1175/JCLI-D-20-0577.1.

Jiang, L.-Z., Fu, S.-M., Sun, J.-H., Fu, R., Li, W.-L., Zhao, S.-X., Wang, H., 2021. Surface wind and vertical extent features of the explosive cyclones in the Northern Hemisphere based on the ERA-I reanalysis data. Int. J. Climatol. 42, 993–1014. doi:10.1002/joc.7284.

Li, X., Pan, Y., Jiang, Y., 2022. The analysis of the spatiotemporal variations and mechanisms for the near-surface wind speed over China in the last 40 years. Theor. Appl. Climatol. 148, 1163–1180. doi:10.1007/s00704-022-03991-z.

Ma, H., Li, G.Q., Zeng, C.K., Wang, F., Jin, S.L., Fu, S.-M., 2022. Evolutionary mechanisms of the strong winds associated with an intense cold wave event and their effects on the wind power production. Front. Earth Sci. 10, 1054037. doi:10.3389/feart.2022.1054037.

Markowski, P.M., Richardson, Y.P., 2010. Mesoscale meteorology in midlatitudes. Wiley-Blackwell, p. 407.

McClung, B., Mass, C.F., 2020. The strong, dry winds of central and northern California: Climatology and synoptic evolution. Wea. Forecast. 35, 2163–2178. doi:10.1175/WAF-D-19-0221.1.

Nan, Y., Liu, P., Wang, W., Chen, Y., 2024. Comparative study on climate characteristics of daily mean wind and daily extreme wind throughout China. Arid Zone Res. 41 (9), 1468–1479. doi:10.13866/j.azr.2024.09.04.

Qin, L., Li, Y.-D., Gao, S.-T., 2006. The synoptic and climatic characteristic studies of thunderstorm winds in Beijing. Clim. Environ. Res. 11, 754–762. doi:10.3878/j.issn.1006-9585.2006.06.10, (in Chinese).

Tsai, C.-L., Kim, K., Liou, Y.-C., Kim, J.-H., Lee, Y., Lee, G., 2022. Orographic-induced strong wind associated with a low-pressure system under clear-air condition during ICE-POP 2018. J. Geophys. Res.: Atmos. 127, e2021JD036418. doi:10.1029/2021JD036418.

Tsukada, T., Horinouchi, T., 2023. Strong relationship between eye radius and radius of maximum wind of tropical cyclones. Mon. Wea. Rev. 151, 569–588. doi:10.1175/MWR-D-22-0106.1.

Wagner, M., Coniglio, M., Rasmussen, E., Satrio, M., Bodine, D., Candela, D., Kennedy, D., Tirone, E., 2025. Harnessing UAS and high-resolution satellite imagery to better characterize wind damage and understand tornado behavior. Bull. Am. Meteorol. Soc. 106, E492–E508. doi:10.1175/BAMS-D-23-0234.1.

Walsh, K.J.E., Sharmila, S., Thatcher, M., Wales, S., Utembe, S., Vaughan, A., 2020. Real world and tropical cyclone world. Part II: Sensitivity of tropical cyclone formation to uniform and meridionally varying sea surface temperatures under aquaplanet conditions. J. Clim. 33, 1473–1486. doi:10.1175/JCLI-D-19-0079.1.

Xi, T., Xu, X., Wei, P., Wang, Y., Ming, J., Zhang, S., Ding, J., Abulikemu, A., 2022. On the high winds in the Tianshan Grand Canyon in Northwest China: General features, synoptic conditions, and mesoscale structures. Front. Earth Sci. doi:10.3389/feart.2022.926339.

Yamada, K., Hirasawa, N., 2018. Analysis of a record-breaking strong wind event at Syowa Station in January 2015. J. Geophys. Res.: Atmos. 123, 13643–13657. doi:10.1029/2018JD028877.